Nano Research
https://doi.org/10.1007/s12274-018-1973-4
Research Article
ISSN 1998-0124
CN 11-5974/O4

A temperature-activated nanocomposite metamaterial absorber with a wide tunability

Weiwei Li[1,2,§], Lingyu Zhao[1,2,§], Zhaohe Dai[1], Hao Jin[1] (✉), Feng Duan[1,2], Junchao Liu[1,2], Zhihui Zeng[1], Jun Zhao[1] (✉), and Zhong Zhang[1] (✉)

[1] *CAS Key Laboratory of Nanosystem and Hierarchical Fabrication, CAS Center for Excellence in Nanoscience, National Center for Nanoscience and Technology, Beijing 100190, China*
[2] *University of Chinese Academy of Sciences, Beijing 100149, China*
[§] *Weiwei Li and Lingyu Zhao contributed equally to this work.*

Received: 29 May 2017
Revised: 15 December 2017
Accepted: 28 December 2017

KEYWORDS
composite materials,
flexible electronics,
metamaterials,
polymeric materials,
shape memory polymers

ABSTRACT

Novel thin and flexible broadband electromagnetic microwave absorbers are realized with nanocomposites and achieve a wide frequency tunability (from 10 to 17.2 GHz) by actively adjusting the resistance. The proposed absorbers are fabricated by scalable screen printing of optimized nanoparticle ink onto the flexible dielectric composite substrates. Based on the shape memory effects of the substrate and piezoresistive effect of the nanocomposite frequency selective surface, a controllable sheet resistance, and thereby tunable wave absorption performance, can be realized in a temperature-activated and dynamically stable manner. The results provide new dimensions for the design of active electromagnetic devices by utilizing previously underestimated intrinsic properties of the artificial materials and the smart behavior of polymer-based nanocomposites.

1 Introduction

Electromagnetic wave absorbers have been continuously undergoing rapid development for their essential role in a variety of aerospace, mechanical, and civil systems [1–3]. Although absorbers composed of conventional materials have shown invaluable effects in many electromagnetic systems, they suffer from several disadvantages: They are very thick [4], have a high rigidity, and provide an unsatisfactory performance (e.g., limited resonant frequency and narrow absorption bandwidth). Therefore, sustained and innovative efforts have led to the development of advanced electromagnetic wave absorbers made from artificial materials, e.g., metamaterials and frequency selective surfaces (FSSs), with an exceptional combination of perfect absorption and thin configuration [5–11]. Moreover, the wave absorption performances

Address correspondence to Zhong Zhang, zhong.zhang@nanoctr.cn; Hao Jin, hjin@nanoctr.cn; Jun Zhao, zhaoj@nanoctr.cn

are tunable, allowing the designer to control the resonant frequency and to even achieve broadband properties [3, 12–15]. However, the reported wave absorption performances were passively improved by utilizing phase transition materials to break the impedance matching condition [12], changing the moisture content to determine the permittivity [16], integrating ferrite to adjust the magnetic field [17], and so on. Alternatively, the employed artificial materials are sometimes active. Their intrinsic properties and material behaviors are also tunable (which was previously underestimated), hence representing an active way to tailor and optimize the overall electromagnetic absorption performance.

The concept of active behaviors in materials, especially nanocomposites, is not new, and the mechanisms are often attributed to the prominence of the structural complexity that external stimuli could alter the micro/nanostructures and in turn their bulk properties [18–20]. The most familiar examples are *in vivo* biomaterials, whose structural complexities could achieve various functions, such as mechanical support, motility, and signal sensing, when interacting with natural stresses, temperatures, and electricity. As for biological materials, artificial nanomaterial-based composites featured hierarchical structures because of bottom-up fabrications and hence endowed the macroscopic nanocomposites with an active performance [20–23]. Examples include the extensive reports on nanomaterial-based electromechanical sensors [23] and temperature-, moisture-, and electricity-activated actuators [24, 25]. Moreover, the outstanding physical properties of the building blocks (e.g., various nano-carbons and metal nanowires) further provide the overall nanocomposites with a controllable conductivity, mechanical stability, and multifunctional performance, combining the ideal properties for potential applications in electronics and electromagnetic devices [26, 27]. Consequently, optimal integrations of the intrinsically excellent properties and active behavior offer a new dimension in the design of electromagnetic wave absorbers. However, few reports have addressed the active design of electromagnetic devices.

In this article, we demonstrate a nanocomposite-based absorber with the typically used FSS by integrating multiple components with specific electromechanical properties to achieve an ultra-wide tunability. Based on the shape memory effects of the substrate and piezoresistive effect of the nanocomposites, a tunable sheet resistance (> 200 $\Omega \cdot sq^{-1}$) and wave absorption performance (resonant frequency tunability: > 7 GHz, absorption bandwidth: ~ 11 GHz) could be temperature-activated in a controlled, dynamically stable manner. Theoretical analysis and electromagnetic simulation are carried out to explore and validate the key parameters (e.g., sheet resistance) for microwave absorption of the proposed absorber.

2 Experimental

2.1 Preparation of the polycyclooctene (PCO) composite film

PCO particles were melted in an internal mixer (HAAKE Rheomix 3010 OS) at 70 ℃ for 10 min. The stirring speed was set to 50 rpm after the PCO completely melted. Then, a desirable amount of multi-walled carbon nanotubes (MWCNTs) and a radical initiator (2,5-dimethyl-2,5-di(tert-butylperoxy)-hexane) were added to the melted PCO and mixed by stirring for 20 min to obtain MWCNT/PCO composites. To investigate the dielectric property of the sample, the composites were compressed using a hot press machine at 160 ℃ for 10 min and naturally cooled. For the substrate of the proposed absorber, the temperature of 70 ℃ (above the switch temperature (T_{sw})) was used to model the film under compression of 20 MPa to obtain an uncrosslinked PCO composite film with a thickness of 2 mm.

2.2 Construction of a resistive FSS array and ground plane

Two kinds of inks were prepared to construct the patterns on the uncrosslinked PCO composite film through screen printing. For the resistive FSS array, a silver nanoparticle (AgNP) ink (prepared in laboratory) was mixed with a MWCNT ink (solvent: N-methyl-2-pyrrolidone) and carbon black nanoparticles (CBNPs) by magnetic stirring and ultrasonic treatment until a homogeneous dispersion was obtained. For the ground plane, a commercial Ag microflake ink was mixed

with the MWCNT ink with the assistance of stirring and ultrasonic treatment. The prepared inks were used for screen printing using a nylon template with a mesh number of 250 mesh per inch. The speed of the doctor blade and squeegee was set to 300 mm·s^{-1}. The printed sample was dried naturally without a sintering treatment.

2.3 Fabrication of the absorber based on PCO

The uncrosslinked PCO composite film with a printed resistive FSS array and ground plane was placed in a mold on a plate vulcanizing machine at 160 °C for 20 min under compression of 20 MPa. Then, the sample was quickly cooled to room temperature using water. After peering from the mold, the absorber was obtained and used for further tests.

2.4 Characterizations and analyses

The permittivity of the PCO composite film (22.86 mm × 10.16 mm) was measured in the frequency range of 8.2–12.4 GHz (X-band) within a waveguide method using a vector network analyzer (Agilent E8363B PNA-L). Scanning electron microscopy (SEM) images were obtained using a JEOL SM-J7500F microscope after sputtering a 5-nm-thick gold film. The resistance variation was recorded using a semiconductor test system (Keithley 4200-SCS) with the assistance of a tensile hot stage at 90 °C with a speed of 0.1 mm·s^{-1}. The sheet resistance of the conductive layer was measured using a four-probe measurement system (4-Probes Tech). The shape recovery time (t_r) was evaluated by placing stretched samples (dimensions of approximately 15 mm × 9.5 mm × 2 mm) with a strain of 0.8%–10% on a hot plate at approximately 60 °C. The reflectivity and transmissivity curves of the proposed absorbers were extracted using a vector network analyzer (Agilent E8363B PNA-L) equipped with a pair of standard horn antennas (frequency range: 8–18 GHz).

2.5 Simulation

The commercially available CST Microwave Studio 2014 software was used to simulate the absorption performance of the proposed absorber, and the results are shown in Figs. S7 and S9 in the Electronic Supplementary Material (ESM). One single resistive FSS unit cell was modeled in the simulation process. The periodic boundary conditions are set along the *x*- and *y*-axes, and the electromagnetic wave propagates along the *z*-axis. A 50-μm-thick plate with a conductivity of 2,000 S·m^{-1} was placed on the back side of the unit cell to prevent wave transmission. The dielectric substrate had a thickness of 2 mm and permittivity of $4.1 \pm 0.2j$. The square FSS patch of the unit cell had a periodicity (p) of 4 mm, side length (l) of 3.3 mm, and thickness of 50 μm. During the simulation process, the conductivity of the FSS patch was changed from 2,667 to 78 S·m^{-1} (corresponding to a sheet resistance change from 7.5 to 256 Ω·sq^{-1}). The *S*-parameters (e.g., *S*11 and *S*21) were obtained at a given sheet resistance and used to calculate the reflectivity and transmissivity.

3 Results and discussion

3.1 Scalable fabrication of nanocomposite-based absorbers with shape memory polymers

We first demonstrate the effective and scalable techniques used to fabricate the nanocomposite-based absorbers (Fig. 1). We used specific functional nanomaterials to fabricate the FSS-type absorber, which was typically comprised of three nanocomposite layers—a resistive FSS array, a dielectric substrate, and a ground plane—with optimized electrical properties and without any loss of flexibility. Specifically, the uncrosslinked MWCNT/PCO composite film was fabricated as the substrate layer with a controlled permittivity and thickness. We constructed the large pattern array (thickness: ~ 5 μm) and ground plane (thickness: ~ 5 μm) on either side of the uncrosslinked MWCNT/PCO composite substrate (Fig. 1(a)) using different types of inks, including the self-prepared AgNP/MWCNT/CBNP and commercial Ag microflake/MWCNT composite inks. The ink coating could be effectively performed using the well-developed, scalable, and low-cost screen printing technique. We further compressed the patterned MWCNT/PCO film at 160 °C to complete the crosslinking process and then cooled it with water. The post-crosslinking procedure is very important for interfacial adhesion. As expected, unlike the ink coating on a crosslinked

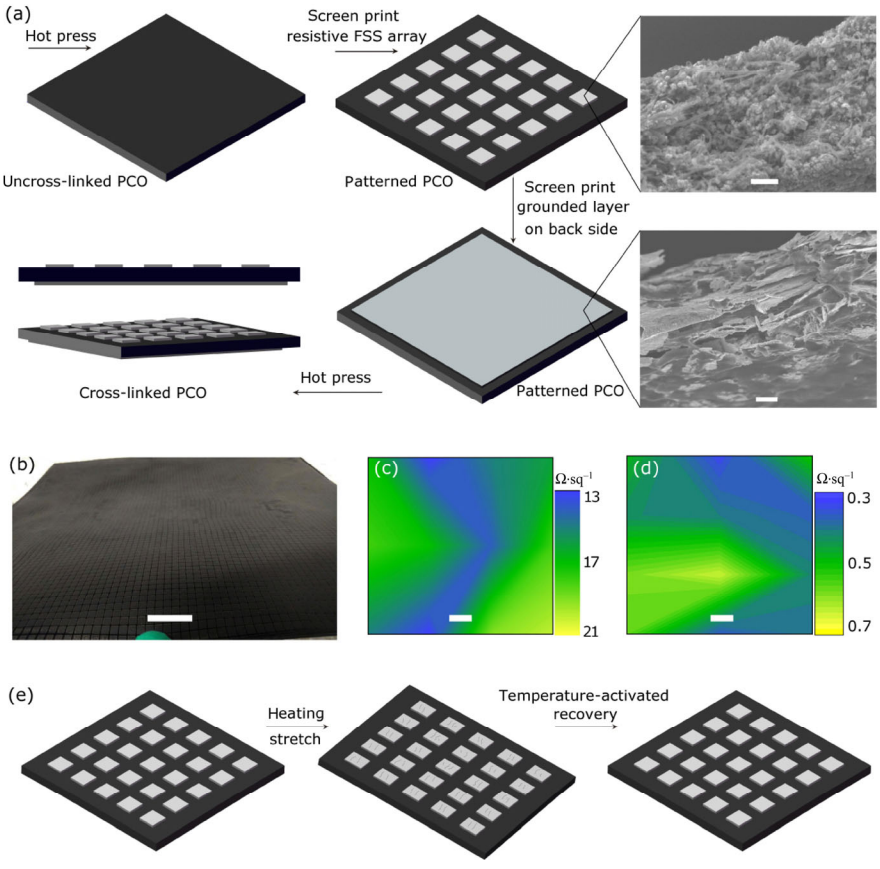

Figure 1 (a) Schematic illustration of the process for fabricating a microwave absorber based on a PCO composite film. The cross-section micromorphologies of the printed layers on both sides of the substrate are shown in the enlarged view. (b) Photograph of the constructed FSS array on the surface of the MWCNT/PCO composite. Scale bar represents 20 mm. (c) and (d) Sheet resistance distribution of the FSS layer and ground plane. Scale bars represent 20 mm. (e) Shape memory effect of the fabricated absorber by stretching at a high temperature, fixing a temporary shape at room temperature, and temperature-activated recovery to the permanent shape.

substrate, our post-crosslinking process exhibits an undiscernible interfacial failure, such as debonding or chipping on the printed patterns, even after 100 stretch-recovery cycles (Figs. S1(a)–S1(c) in the ESM). Benefiting from the screen printing technique and post-crosslinking procedure, the as-prepared 400 mm × 400 mm × 2 mm absorbers with the patterned FSS array (10^4 building blocks) and the uniform ground plane were successfully manufactured (Fig. 1(b)). In addition, the array layers show a uniform sheet resistance distribution after measuring 6 × 6 unit cells, and the averaged value is 16 ± 2.4 Ω·sq^{-1} (Fig. 1(c)). For the 5-μm-thick ground planes, such uniformity could also be observed in Fig. 1(d), and we also achieved an excellent conductivity (sheet resistance of 0.45 ± 0.12 Ω·sq^{-1}), preventing wave transmission out of the absorber (Fig. S2(a) in the ESM) and guaranteeing high-performance wave absorption (Fig. S2(b) in the ESM).

Then, the active strategies to tune the wave absorption performance, including our novel demonstrations, are introduced. The passive tunability is widely used by modifying the impedance condition, geometry size, and shape of the surface patterns and by employing a substrate with a different permittivity; this could be readily achieved by our fabrication procedure and design of nanocomposites (as illustrated later). Considering that the nanocomposites feature hierarchical microstructures and thus endow electro-mechanical behaviors that are extensively explored in nanocomposite-based conductors, actuators, and sensors [18–27], we can readily utilize these smart properties and intrinsically tune the sheet resistance of our composite-based components. We hence

examined the electrical response of our absorbers to mechanical deformation, which is believed to trigger an electro-mechanical coupling mechanism for a nanocomposite with conductive fillers and then allow for control of the resistance and wave absorption performance with the aid of deformations. We applied the deformation onto the overall structures through the temperature-activated method by utilizing the shape memory effects of our PCO-based substrate in Fig. 1(e). Shape memory polymers (SMPs) can proceed to permanent shapes from a temporary shape in response to various external stimuli, such as light, heat, pH, pressure, and electric field [28–30]. SMPs are different from elastomeric rubbers and other stretchable substrates, which require a continuous mechanical force to maintain a stable status [31, 32] and can retain their temporary shape even after unloading the stimulus. Temperature-activated recovery to a permanent shape can be observed when the stimulus is reloaded. PCO, as a widely used SMP material, has a relatively low T_{sw}, which is sufficient to utilize the shape memory effect around 60 °C, and the recoverable strain could be up to 730% [33], offering an active method to control the deformation and absorption performance of our nanocomposite system.

3.2 Nanocomposites with controllable properties

We focused on the previously underestimated deformation-induced resistance and absorption tunability. The PCO substrate has a large stretchability (~ 700%), but only 10% strain was used to rule out the effect of Poisson's ratio (~ 0.51 for the substrate, see Fig. S3(a) in the ESM) on the absorption performance (Fig. S3(b) in the ESM) and explore the resistance effects in a controlled manner. We first measured the electrical properties of our nanocomposite-based components (i.e., substrate, ground plane, and surface FSS array) when subjected to strains (Fig. 2), which also provides valuable guidelines for the nanocomposites design with optimal functional fillers and performances. For the substrate layers, the permittivity is one of the most important properties that affects the overall wave absorption performance. The original PCO, which shows an excellent shape memory and deformation controllability, always shows a poor permittivity (dielectric constant of approximately 2.3 in the X-band). After carefully comparing the typically used nanofillers, such as inorganic nanoparticles [34] and two-dimensional graphene sheets (Fig. S4 in the ESM) [35, 36], we employed one-dimensional fillers, the MWCNTs, to improve the permittivity of the PCO film. Figure 2(a) shows that the permittivity of the PCO composites could be effectively increased to 4.1 after only introducing 0.2 wt.% MWCNTs into the substrate, and the permittivity can reach 11 with 1 wt.% MWCNT fillers. In the following demonstrations, PCO composites with 0.2 wt.% MWCNTs are used to consider the possible compromise in mechanical properties at high-level content. Moreover, the high permittivity of our MWCNT/PCO nanocomposites could nearly be maintained to around 4.1 when undergoing a 10% stretching strain (Fig. 2(b)).

For the ground planes, high conductivity after deformation is essential to prevent wave transmission and guarantee high-performance wave absorption. For this purpose, we blended MWCNTs in commercially available Ag microflake ink, which offers additional conducting paths for the as-printed ground plane, according to SEM observation (Fig. 1(a) and Fig. S5 in the ESM). Consequently, *in situ* electro-mechanical tests (see Fig. 2(c) and the Experimental Section) indicate that the sheet resistance of our composite ground plane stably varies from 0.8 to 7.2 $\Omega \cdot sq^{-1}$ under an applied strain of 10% (which is efficient for electromagnetic devices). We further reveal the generated Joule heat of this highly conductive layer (Fig. 2(d)): The relatively uniform temperature distribution increased gradually to 50 °C under a direct current (DC) voltage of 17 V within 10 min and further reached 60 °C under 21 V (this temperature is above the T_{sw} of the PCO film). This result implies that we could also employ a high-conductivity ground plane as a heater to activate the stretch–recovery process of the SMP substrate (Fig. 2(e)). The temperature-induced shape recovery effect (t_r) was investigated at 60 °C (Fig. S1(d) in the ESM). The value of t_r increases with increased mechanical loading. The stretched sample could recover from storage within 60 s with an applied strain of 9.2%. If a higher temperature is achieved by increasing the DC voltage, the recovery time might be correspondingly short.

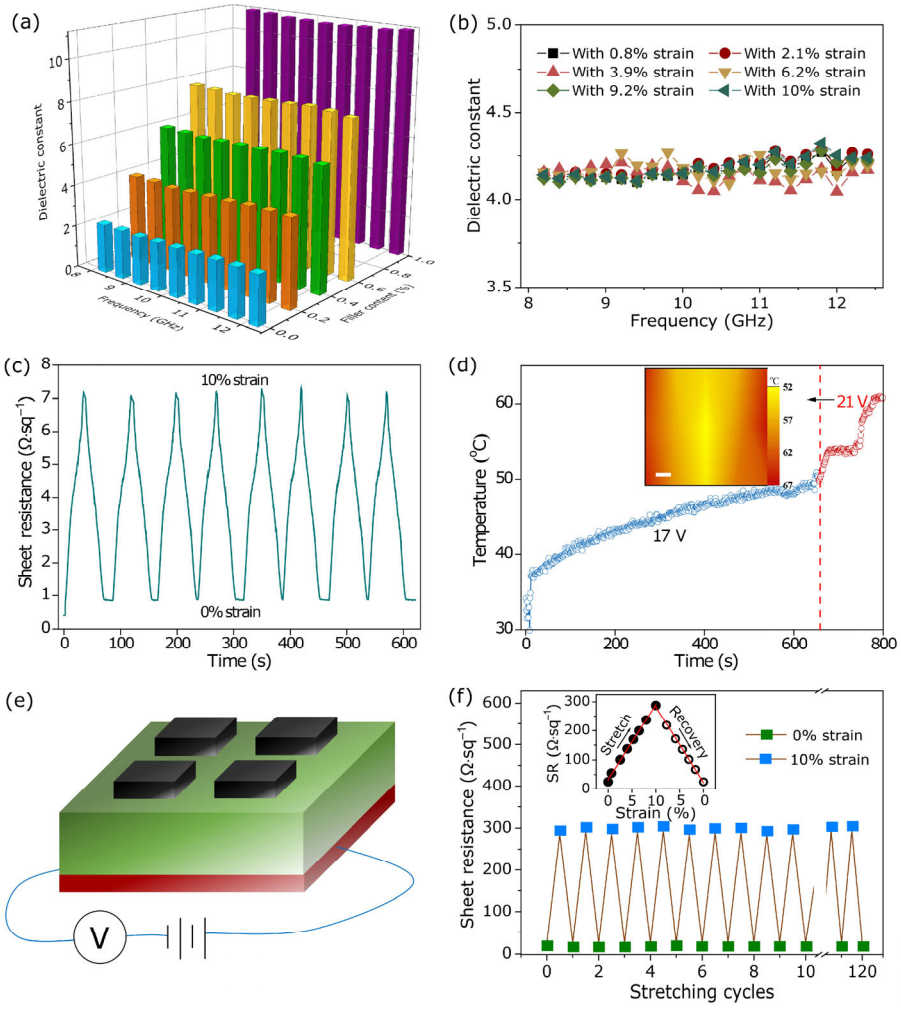

Figure 2 Dielectric constant of (a) pure PCO and its composites with different amounts of MWCNTs, and (b) MWCNT/PCO nanocomposites (with 0.2 wt.% filler) under strains of 0.8%, 2.1%, 3.9%, 6.2%, 9.2%, and 10%. (c) Sheet resistance of the ground plane during stretch–recovery cycles under a 10% strain. (d) Joule heat of the highly conductive ground plane under DC voltages of 17 and 21 V. The inset shows the temperature distribution after 800 s. Scale bar represents 5 cm. (e) A schematic illustration of the working principle of the absorber under an applied voltage to the ground plane. (f) The dependence of the sheet resistance of the FSS array on the stretching cycles under a 10% strain. Inset shows a plot of the detailed sheet resistance variation versus the strain during one stretch (filled) and recovery (open) cycle. The red lines are a linear fit of the stretch and recovery processes, with coefficient of determination (R^2) values of 0.997 and 0.998, respectively.

The electrical properties and geometry of the FSS array are key to the entire wave absorption performances, i.e., the frequency and bandwidth. Moreover, both parameters can also be passively adjusted in our procedures to tune the wave absorption performances of the nanocomposite absorber. For instance, we fabricated this array by screen printing a composite ink; a variety of geometries could be effectively and scalably achieved using this method. Meanwhile, the electrical/electromechanical properties of the nanocomposites can also be tuned by the compositions or the multi-scale structures. Here, to achieve an active, ultra-wide tunability of the wave absorption frequency, an FSS array with a large, stable sheet resistance response with respect to deformation (less than 10% strain) would be important. We compared a sample with a different portion of nanofillers (Fig. S6 in the ESM) and multilayered structures (Fig. S7 in the ESM). By considering the microstructural homogeneity, conductivity, and electromechanical performance, we printed a single, uniform layer using a AgNP/MWCNT/CBNP composite ink (10:1:0.035). By utilizing

the temperature-activated shape memory effects of the substrate to transfer the deformation onto the FSS array, we measured the variation of the sheet resistance of our FSS array in a tensile hot stage at 90 ℃ (Fig. S1(a) in the ESM). Figure 2(f) demonstrates that the optimized array shows a large sheet resistance change from 25 to approximately 280 $\Omega \cdot sq^{-1}$ when a dynamic tension strain of 10% is applied. Such electromechanical coupling behavior is repeatable, even after more than 100 cycles (Fig. S1(b) in the ESM). Moreover, the nanocomposite conductive layer shows an excellent stability after evaluating the variation in the sheet resistance after exposure to ambient atmosphere for more than 7 months (Fig. S1(c) in the ESM). These behaviors lead to a potential in the temperature-activated, nanocomposite-based microwave absorber with a wide and durable tunability.

3.3 Broadband microwave absorption with an active, ultra-wide tunability

Benefiting from the high conductivity of the ground plane and the shape memory effect of the substrate, we can control the deformation and sheet resistance of the FSS array by applying a voltage, as shown in Fig. 3(a). After applying the voltage to heat the sample, the substrate recovery could be activated and transferred to the arrays. A temporary shape could be retained after removing the applied voltage to cool

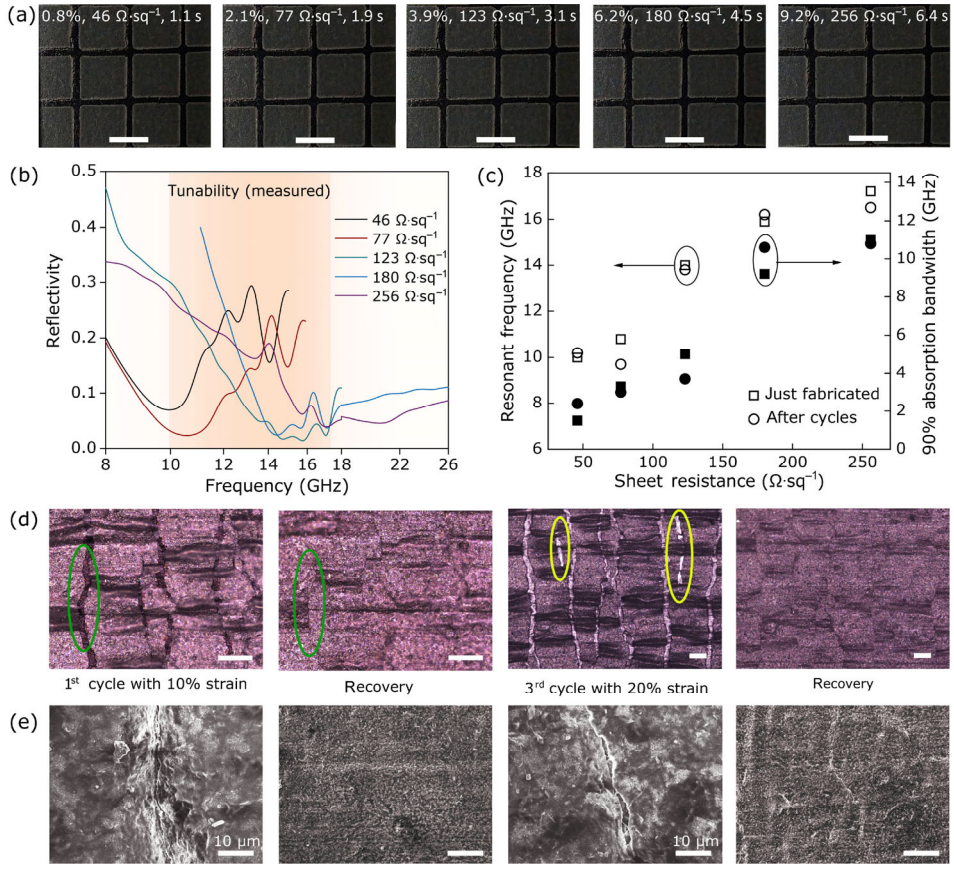

Figure 3 (a) Optical photographs of the FSS array under different strains above T_{sw}. The patterns become wider along the stretching axis with increasing applied strain, and the scale bars represent 3 mm. (b) Summary of the five measured spectra with different sheet resistance values, indicating a shift of the resonant frequency and broadening of the absorption bandwidth. The color represents the experimental tunability (up to 7.2 GHz from 10 to 17.2 GHz for the resonant frequency) of the fabricated absorber. (c) Sheet resistance dependence of the corresponding resonant frequency (open interior), and 90% absorption bandwidth (solid interior) of the fabricated absorber before (squares) and after (circles) the stretch–recovery cycles. (d) Optical images of the resistive FSS with different stretch–recovery cycles and different strains. The green cycles indicate the gap between cracks under 10% strain and 0% strain. The yellow circles indicate new cracks after a 20% strain is applied to the substrate. (e) The corresponding SEM images of the FSS layer under a 10% strain, recovery, 20% strain, and recovery. All scale bars represent 100 μm.

the SMPs to 30 °C before releasing the mechanical stress. Consequently, the strain of the structures could be controlled, one-way adjusted, and the increased sheet resistance, as well as the resulted wave absorption performance, could be simultaneously measured. The free-space measurement system was used to investigate the absorption performance of the fabricated absorber. Figure 3(b) shows five typically measured reflectivity curves with sheet resistances of 46, 77, 123, 180, and 256 $\Omega \cdot sq^{-1}$. The minimum values of the reflectivity, which are regarded as the resonant frequency of the proposed absorber, shift to higher frequencies with increasing sheet resistance. Specifically, the relevant resonant frequency is 10 GHz at 46 $\Omega \cdot sq^{-1}$, 10.8 GHz at 77 $\Omega \cdot sq^{-1}$, 14 GHz at 123 $\Omega \cdot sq^{-1}$, 15.9 GHz at 180 $\Omega \cdot sq^{-1}$, and 17.2 GHz at 256 $\Omega \cdot sq^{-1}$. Similar simulation results can also be observed in Fig. S8 in the ESM. The tunability of the measured frequency can reach 7.2 GHz, which is much wider than that for recently reported tunable absorbers, such as the absorber of liquid metal combined with a stretchable substrate (0.15 GHz) [37], liquid-crystal-based absorber (0.17 GHz) [38], magnetically tunable ferrite-based absorber (0.28 GHz) [17], mechanical stress tunable absorber (0.41 GHz) [31], microfluid absorber (0.45 GHz) [39], and p-type/intrinsic/n-type (PIN) diode-based FSS absorber (1.3 GHz in the range of 1–4 GHz) [3]. In addition, our absorber also exhibits a broadband absorption performance; the measured 90% absorption bandwidth (corresponding to a reflectivity below 0.1) increases from 1.5 to 11 GHz, which is broader than most reported bandwidths for a similar thickness, such as a square ring FSS array based absorber (3 mm with 6 GHz) [40], dentric resistive FSS film-based absorber (2 mm with 7.5 GHz) [41], and periodic pattern surface-based absorber (3 mm with 4.2 GHz) [42].

We further examined the stability and repeatability of the frequency tunability. The absorber recovered to its original shape after removing the stress that was applied to the MWCNT/PCO composite film; we conducted more than 10 stretch–recovery cycles at a strain of 10%. The substrate was then stretched gradually to the strain level applied in the first cycle, and the absorption performance was measured. The reflectivity spectra before and after the stretch–recovery cycles are shown in Fig. S9 in the ESM and summarized in Fig. 3(c). Both the sheet resistance dependence of the resonant frequency and the 90% absorption bandwidth reflectivity after dynamic cycles show nearly identical performances during the first cycle (Fig. 3(b)), indicating the excellent stability and durability of our nanocomposite-based absorber. Such repeatability should be attributed to the stable electromechanical performance of the FSS array (Fig. 2(f)), which is called the piezoresistive effect of nanocomposites with conductive nanofillers [22]. We further present an in-depth study of the piezoresistive effect in terms of the structural deformation (optical images in Fig. 3(d) and SEM images in Fig. 3(e)). We suggest that the increase in the sheet resistance is caused by the 10% tensile strains, which can induce localized deformation of the microstructure and possibly increase the contact distance (tunneling conduction theory) between the connected conductive fillers and synergistically reduce the number of conductive paths within the microstructures. Figures 3(d) and 3(e) demonstrate that once the load is removed, the microstructure of the nanocomposite array returns to the pre-stretched configurations, allowing them to spring back to their original shape and resistance. Interestingly, these mechanisms can also be observed under a strain of 20% (Figs. 3(d) and 3(e)), implying a possible larger sheet resistance change and wider frequency tunability without a loss in stability.

3.4 Theoretical analysis and simulations

To clarify the underlying mechanism for our observed ultra-wide tunability, we present simulations and analysis of the absorbing structure by a simple equivalent circuit that allows a detailed explanation of the key parameters (including the tunable sheet resistance in our experiments) for the design of the absorber. Figure 4(a) shows the proposed metal-substrate-metal structure of the microwave absorber. The resistive square array with a sheet resistance of R_{sq} and geometry parameters (i.e., side length l and periodicity p) were used as a unit cell of the FSS in our design. A dielectric layer with thickness d, permittivity ε_r, and permeability μ_r was interbedded between the FSS arrays and ground plane. The corresponding equivalent circuit model of the proposed absorber is illustrated in Fig. 4(b). According to the

equivalent circuit theory, the expressed impedance should match the free space impedance to obtain a perfect absorption of the incoming signal. Thus, the optimal sheet resistance can be obtained as

$$R_{sq} = \frac{377 \tan^2(2\pi fd\sqrt{\varepsilon_r}/c)}{\tan^2(2\pi fd\sqrt{\varepsilon_r}/c) + \varepsilon_r}\left(\frac{l}{p}\right)^2 \quad (1)$$

where f is the frequency of the incident wave, c is the speed of light in a vacuum (refer to Section S1 in the ESM) [5, 43, 44]. In addition, we also employed the commercial CST Microwave Studio 2014 software to simulate the absorption performance of the resistive FSS unit cell used in our experiments (refer to the Experimental Section and Figs. S2 and S10 in the ESM).

Equation (1) highlights the dependence of the optimal FSS resistance on the thickness and permittivity of the substrate. Unlike modifying the geometry parameters (e.g., l and p) and properties of the substrate (e.g., ε_r and μ_r), as done in previous reports (refer to the Introduction), we focused on the tunability of the microwave absorber based on the R_{sq}. According to our fabrication details (Experimental Section), we employed a dielectric substrate with a thickness of 2 mm, effective permittivity of 4.1, and geometry parameters of the unit cell of p = 4 mm and l = 3.3 mm for the calculations and simulations. Figure 4(c) shows that the f increases gradually with the sheet resistance, which is similar to the measured tunability. Specifically, when we changed the sheet resistance from 7.5 to 256 Ω·sq^{-1} (Figs. 2(f) and 4(c)), a calculated tunability of the resonant frequency with a range of about 15 GHz (from 4 to 19 GHz, square symbols in Fig. 4(c)) can be expected, which strongly agrees with our experiments (Fig. 3(b)), and is far beyond the results of previous reports [3, 16, 17]. In addition, the single resonant characteristic of the proposed structure throughout the 4–19 GHz range implies a single absorption peak

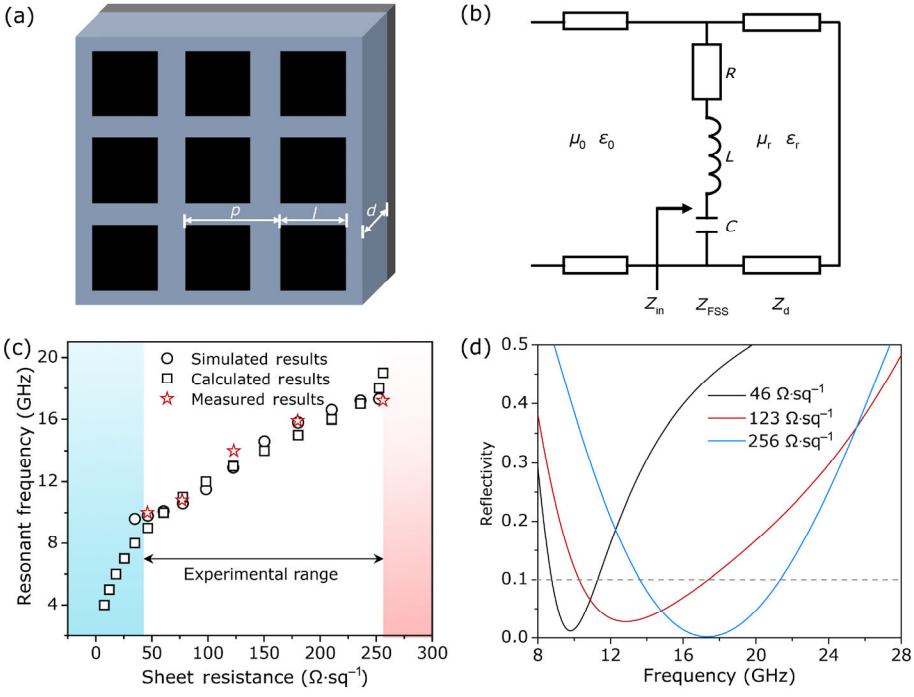

Figure 4 (a) The designed absorber with a tunable frequency based on the resistive FSS. (a) A three-dimensional illustration of the proposed structure. p is the periodicity of the unit cell, l is the side length of the FSS array, and d is the thickness of the substrate. (b) Sketch map of the equivalent circuit model. Z_{in}, Z_{FSS}, and Z_d are the input impedance of the proposed absorber, the equivalent impedance of the resistive FSS array, and grounded dielectric substrate, respectively. R, L, and C are the equivalent resistance, inductance, and capacitance of the resistive FSS, respectively. (c) Simulated (circles), calculated (squares), and measured (stars) resonant frequencies as a function of the optimal sheet resistance. Colored backgrounds indicate the predicted data acquired from Eq. (1). (d) The numerically simulated reflectivity curves of the FSS absorber with three typical sheet resistances indicating the shift of the resonant frequency and broadening of the absorption bandwidth.

in the resonant frequency. Similar results can also be observed in our electromagnetic simulation (circle symbols in Fig. 4(c)) and experimental measurement (star symbols in Fig. 4(c)). The simulated and measured resonant frequencies under different sheet resistances agree with our calculated results (Fig. 4(c)). Specifically, in Fig. 4(d), the simulated reflectivity curves with three typical sheet resistances of 46, 123, and 256 $\Omega \cdot sq^{-1}$ reveal the shifts of the resonant frequency of 9.6, 12.9, and 17.4 GHz, respectively, which are consistent with the wide tunability in our experiments. In addition, a broader band of absorption performance could also be observed (e.g., 90% absorption bandwidths are 2.6, 6.9, and 7.7 GHz). Our theoretical analysis and simulations could clearly validate the parameter of sheet resistance used in the experiments and lead to the promising potential of sheet resistance in achieving an ultra-wide and controllable tunability of broadband microwave absorption.

4 Conclusions

A novel frequency-tunable absorber based on temperature-activated nanocomposite layers has been developed. The resistive FSS array was constructed on a PCO/MWCNT composite film with a desirable permittivity and thickness. By applying a small strain (e.g., 10%) to the substrate below 60 ℃, the deformation varies the sheet resistance, and the absorption performance can be tuned with an ultra-wide range because of the dependence of the resonant frequency and absorption bandwidth on the sheet resistance. With insignificant deviations between the measured and simulated results, our proposed absorber exhibited a frequency tunability of 7.2 GHz. Moreover, 90% of the absorption bandwidth of the absorber reaches 11 GHz, while the thickness is only 2 mm. Our absorbers also show an excellent stability after several stretch–recovery cycles. Through theoretical analysis and simulations, the experimental results can be clearly validated, and the promising potential in achieving an ultra-wide and controllable tunability of broadband microwave absorption can also be achieved. The novel design concept and excellent performance are expected to open new opportunities for practical applications of the electromagnetic absorber, interference shielding, and stealth.

Acknowledgements

This project was jointly supported by the National Basic Research Program of China (No. 2013CB934203), the "Strategic Priority Research Program" of the Chinese Academy of Sciences (No. XDA09030200), and the National Natural Science Foundation of China (No. 11225210).

Electronic Supplementary Material: Supplementary material (the test setup of sheet resistance, strain of PCO composites, SEM images and sheet resistance of the printed layers, simulated and measured reflectivity spectra, analysis of equivalent impedance, and detailed simulation) is available in the online version of this article at https://doi.org/10.1007/s12274-018-1973-4.

References

[1] Choi, W.-H.; Kim, J.-B.; Shin, J.-H.; Song, T.-H.; Lee, W.-J.; Joo, Y.-S.; Kim, C.-G. Circuit-analog (CA) type of radar absorbing composite leading-edge for wing-shaped structure in X-band: Practical approach from design to fabrication. *Compos. Sci. Technol.* **2014**, *105*, 96–101.

[2] Namai, A.; Sakurai, S.; Nakajima, M.; Suemoto, T.; Matsumoto, K.; Goto, M.; Sasaki, S.; Ohkoshi, S.-I. Synthesis of an electromagnetic wave absorber for high-speed wireless communication. *J. Am. Chem. Soc.* **2009**, *131*, 1170–1173.

[3] Wang, H.; Kong, P.; Cheng, W. T.; Bao, W. Z.; Yu, X. W.; Miao, L.; Jiang, J. J. Broadband tunability of polarization-insensitive absorber based on frequency selective surface. *Sci. Rep.* **2016**, *6*, 23081.

[4] Pang, Y. Q.; Cheng, H. F.; Zhou, Y. J.; Wang, J. Analysis and enhancement of the bandwidth of ultrathin absorbers based on high-impedance surfaces. *J. Phys. D: Appl. Phys.* **2012**, *45*, 215104.

[5] Costa, F.; Monorchio, A.; Manara, G. Analysis and design of ultra thin electromagnetic absorbers comprising resistively loaded high impedance surfaces. *IEEE Trans. Antennas Propag.* **2010**, *58*, 1551–1558.

[6] Ding, F.; Cui, Y. X.; Ge, X. C.; Jin, Y.; He, S. L. Ultra-broadband microwave metamaterial absorber. *Appl. Phys. Lett.* **2012**, *100*, 103506.

[7] Park, J. W.; Van Tuong, P.; Rhee, J. Y.; Kim, K. W.; Jang,

W. H.; Choi, E. H.; Chen, L. Y.; Lee, Y. Multi-band metamaterial absorber based on the arrangement of donut-type resonators. *Opt. Express* **2013**, *21*, 9691–9702.

[8] Xiong, H.; Hong, J.-S.; Luo, C.-M.; Zhong, L.-L. An ultrathin and broadband metamaterial absorber using multi-layer structures. *J. Appl. Phys.* **2013**, *114*, 064109.

[9] Ghosh, S.; Bhattacharyya, S.; Kaiprath, Y.; Srivastava, K. V. Bandwidth-enhanced polarization-insensitive microwave metamaterial absorber and its equivalent circuit model. *J. Appl. Phys.* **2014**, *115*, 104503.

[10] Landy, N. I.; Sajuyigbe, S.; Mock, J. J.; Smith, D. R.; Padilla, W. J. Perfect metamaterial absorber. *Phys. Rev. Lett.* **2008**, *100*, 207402.

[11] Watts, C. M.; Liu, X. L.; Padilla, W. J. Metamaterial electromagnetic wave absorbers. *Adv. Mater.* **2012**, *24*, OP98–OP120.

[12] Wen, Q. Y.; Zhang, H. W.; Yang, Q. H.; Chen, Z.; Long, Y.; Jing, Y. L.; Lin, Y.; Zhang, P. X. A tunable hybrid metamaterial absorber based on vanadium oxide films. *J. Phys. D: Appl. Phys.* **2012**, *45*, 235106.

[13] Kong, P.; Yu, X. W.; Liu, Z. Y.; Zhou, K.; He, Y.; Miao, L.; Jiang, J. J. A novel tunable frequency selective surface absorber with dual-DOF for broadband applications. *Opt Express* **2014**, *22*, 30217–30224.

[14] Li, S. J.; Gao, J.; Cao, X. Y.; Li, W. Q.; Zhang, Z.; Zhang, D. Wideband, thin, and polarization-insensitive perfect absorber based the double octagonal rings metamaterials and lumped resistances. *J. Appl. Phys.* **2014**, *116*, 043710.

[15] Huang, X. J.; He, X. L.; Guo, L. Y.; Yi, Y. Y.; Xiao, B. X.; Yang, H. L. Analysis of ultra-broadband metamaterial absorber based on simplified multi-reflection interference theory. *J. Opt.* **2015**, *17*, 055101.

[16] Ling, K. Y.; Yoo, M.; Lim, S. Frequency tunable metamaterial absorber using hygroscopicity of nature cork. *IEEE Antennas Wirel. Propag. Lett.* **2015**, *14*, 1598–1601.

[17] Huang, Y. J.; Wen, G. J.; Zhu, W. R.; Li, J.; Si, L.-M.; Premaratne, M. Experimental demonstration of a magnetically tunable ferrite based metamaterial absorber. *Opt. Express* **2014**, *22*, 16408–16417.

[18] Liu, Q.; Liu, L. Q.; Xie, K.; Meng, Y. N.; Wu, H. P.; Wang, G. R.; Dai, Z. H.; Wei, Z. X.; Zhang, Z. Synergistic effect of a r-GO/PANI nanocomposite electrode based air working ionic actuator with a large actuation stroke and long-term durability. *J. Mater. Chem. A* **2015**, *3*, 8380–8388.

[19] Kuang, J.; Dai, Z. H.; Liu, L. Q.; Yang, Z.; Jin, M.; Zhang, Z. Synergistic effects from graphene and carbon nanotubes endow ordered hierarchical structure foams with a combination of compressibility, super-elasticity and stability and potential application as pressure sensors. *Nanoscale* **2015**, *7*, 9252–9260.

[20] Lv, T.; Cheng, Z. J.; Zhang, D. J.; Zhang, E. S.; Zhao, Q. L.; Liu, Y. Y.; Jiang, L. Superhydrophobic surface with shape memory micro/nanostructure and its application in rewritable chip for droplet storage. *ACS Nano* **2016**, *10*, 9379–9386.

[21] Dai, Z. H.; Gao, Y.; Liu, L. Q.; Pötschke, P.; Yang, J. L.; Zhang, Z. Creep-resistant behavior of MWCNT-polycarbonate melt spun nanocomposite fibers at elevated temperature. *Polymer* **2013**, *54*, 3723–3729.

[22] Dai, Z. H.; Liu, L. Q.; Qi, X. Y.; Kuang, J.; Wei, Y. G.; Zhu, H. W.; Zhang, Z. Three-dimensional sponges with super mechanical stability: Harnessing true elasticity of individual carbon nanotubes in macroscopic architectures. *Sci. Rep.* **2016**, *6*, 18930.

[23] Dai, Z. H.; Weng, C. X.; Liu, L. Q.; Hou, Y.; Zhao, X. L.; Kuang, J.; Shi, J. D.; Wei, Y. G.; Lou, J.; Zhang, Z. Multifunctional polymer-based graphene foams with buckled structure and negative poisson's ratio. *Sci. Rep.* **2016**, *6*, 32989.

[24] Baughman, R. H.; Cui, C. X.; Zakhidov, A. A.; Iqbal, Z.; Barisci, J. N.; Spinks, G. M.; Wallace, G. G.; Mazzoldi, A.; De Rossi, D.; Rinzler, A. G. et al. Carbon nanotube actuators. *Science* **1999**, *284*, 1340–1344.

[25] Dai, Z. H.; Wang, Y. L.; Liu, L. Q.; Liu, X. L.; Tan, P. H.; Xu, Z. P.; Kuang, J.; Liu, Q.; Lou, J.; Zhang, Z. Hierarchical graphene-based films with dynamic self-stiffening for biomimetic artificial muscle. *Adv. Funct. Mater.* **2016**, *26*, 7003–7010.

[26] Dai, Z. H.; Wang, G. R.; Liu, L. Q.; Hou, Y.; Wei, Y. G.; Zhang, Z. Mechanical behavior and properties of hydrogen bonded graphene/polymer nano-interfaces. *Compos. Sci. Technol.* **2016**, *136*, 1–9.

[27] Wang, G. R.; Dai, Z. H.; Liu, L. Q.; Hu, H.; Dai, Q.; Zhang, Z. Tuning the interfacial mechanical behaviors of monolayer graphene/PMMA nanocomposites. *ACS Appl. Mater. Interfaces* **2016**, *8*, 22554–22562.

[28] Gall, K.; Dunn, M. L.; Liu, Y. P.; Finch, D.; Lake, M.; Munshi, N. A. Shape memory polymer nanocomposites. *Acta Mater.* **2002**, *50*, 5115–5126.

[29] Xu, H. X.; Yu, C. J.; Wang, S. D.; Malyarchuk, V.; Xie, T.; Rogers, J. A. Deformable, programmable, and shape-memorizing micro-optics. *Adv. Funct. Mater.* **2013**, *23*, 3299–3306.

[30] Fang, Y.; Ni, Y. L.; Leo, S.-Y.; Taylor, C.; Basile, V.; Jiang, P. Reconfigurable photonic crystals enabled by pressure-responsive shape-memory polymers. *Nat. Commun.* **2015**, *6*, 7416.

[31] Zhang, F. L.; Feng, S. Q.; Qiu, K. P.; Liu, Z. J.; Fan, Y. C.; Zhang, W. H.; Zhao, Q.; Zhou, J. Mechanically stretchable

and tunable metamaterial absorber. *Appl. Phys. Lett.* **2015**, *106*, 091907.

[32] Yang, S. M.; Liu, P.; Yang, M. D.; Wang, Q. G.; Song, J. M.; Dong, L. From flexible and stretchable meta-atom to metamaterial: A wearable microwave meta-skin with tunable frequency selective and cloaking effects. *Sci. Rep.* **2016**, *6*, 21921.

[33] Zhao, L. Y.; Zhao, J.; Liu, Y. Y.; Guo, Y. F.; Zhang, L. P.; Chen, Z.; Zhang, H.; Zhang, Z. Continuously tunable wettability by using surface patterned shape memory polymers with giant deformability. *Small* **2016**, *12*, 3327–3333.

[34] Inui, T.; Koga, H.; Nogi, M.; Komoda, N.; Suganuma, K. A Miniaturized flexible antenna printed on a high dielectric constant nanopaper composite. *Adv. Mater.* **2015**, *27*, 1112–1116.

[35] Qing, Y. C.; Min, D. D.; Zhou, Y. Y.; Luo, F.; Zhou, W. C. Graphene nanosheet- and flake carbonyl iron particle-filled epoxy–silicone composites as thin–thickness and wide-bandwidth microwave absorber. *Carbon* **2015**, *86*, 98–107.

[36] Feng, J.; Pu, F. Z.; Li, Z. X.; Li, X. H.; Hu, X. Y.; Bai, J. T. Interfacial interactions and synergistic effect of CoNi nanocrystals and nitrogen-doped graphene in a composite microwave absorber. *Carbon* **2016**, *104*, 214–225.

[37] Kim, K.; Lee, D.; Eom, S.; Lim, S. Stretchable metamaterial absorber using liquid metal-filled polydimethylsiloxane (PDMS). *Sensors* **2016**, *16*, 521.

[38] Fusco, V. F.; Cahill, R.; Hu, W.; Simms, S. Ultra-thin tunable microwave absorber using liquid crystals. *Electron. Lett.* **2008**, *44*, 37–38.

[39] Ling, K. Y.; Yoo, M.; Su, W. J.; Kim, K.; Cook, B.; Tentzeris, M. M.; Lim, S. Microfluidic tunable inkjet-printed metamaterial absorber on paper. *Opt. Express* **2015**, *23*, 110–120.

[40] Silva, M. W. B.; Campos, A. L. P. S.; Kretly, L. C. Design of thin microwave absorbers using lossy frequency selective surfaces. *Microwave Opt. Technol. Lett.* **2015**, *57*, 928–933.

[41] Wang, B.; Gong, B. Y.; Wang, M.; Weng, B.; Zhao, X. P. Dendritic wideband metamaterial absorber based on resistance film. *Appl. Phys. A* **2015**, *118*, 1559–1563.

[42] Jang, H.-K.; Choi, W.-H.; Kim, C.-G.; Kim, J.-B.; Lim, D.-W. Manufacture and characterization of stealth wind turbine blade with periodic pattern surface for reducing radar interference. *Composites Part B* **2014**, *56*, 178–183.

[43] Pang, Y.-Q.; Zhou, Y.-J.; Wang, J. Equivalent circuit method analysis of the influence of frequency selective surface resistance on the frequency response of metamaterial absorbers. *J. Appl. Phys.* **2011**, *110*, 023704.

[44] Zhang, G. R.; Zhou, P. H.; Zhang, H. B.; Zhang, L. B.; Xie, J. L.; Deng, L. J. Analysis and design of triple-band high-impedance surface absorber with periodic diversified impedance. *J. Appl. Phys.* **2013**, *114*, 164103.